Electronic Supplementary Information (ESI) for

Novel folic acid complex derived nitrogen and nickel co-doped carbon nanotubes with embedded Ni nanoparticles as efficient electrocatalysts for CO_2 reduction

Xuewan Wang[a], Dan Wu[a], Chengzhi Dai[a], Chenyu Xu[b], Pengfei Sui[b], Renfei Feng[c], Yinping Wei[d], Xian-Zhu Fu*[a] and Jing-Li Luo*[ab]

[a] *College of Materials Science and Engineering, Shenzhen University, Shenzhen 518060, China. Email: xz.fu@szu.edu.cn (X.Z. Fu)*

[b] *Department of Chemical and Materials Engineering, University of Alberta, Edmonton, Alberta T6G 1H9, Canada. Email: Jingli.Luo@ualberta.ca (J.L. Luo)*

[c] *Canadian Light Source Inc., Saskatoon, S7N 0X4, Saskatchewan, Canada*

[d] *Electron Microscopy Laboratory, Materials and Devices Testing center, Graduate School at Shenzhen, Tsinghua University, Shenzhen 518055, China*

Corresponding author

Email: xz.fu@szu.edu.cn (X.Z. Fu)

Email: Jingli.Luo@ualberta.ca (J.L. Luo)

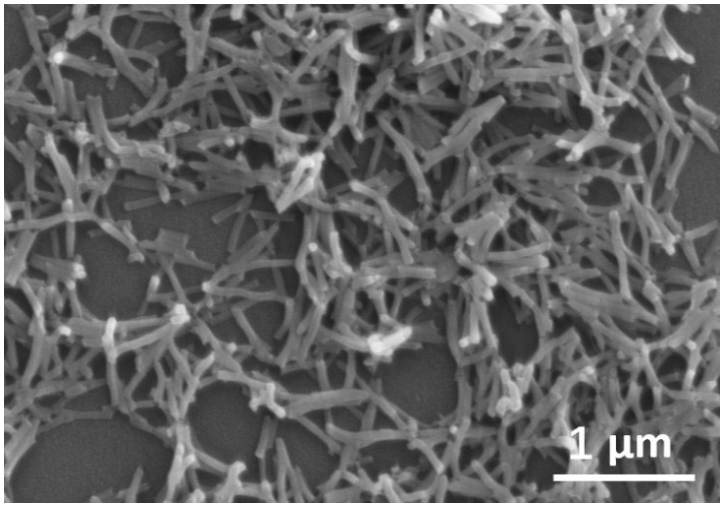

Fig. S1 SEM image of Ni-FA complex nanotubes after a 10 min ultrasonication treatment.

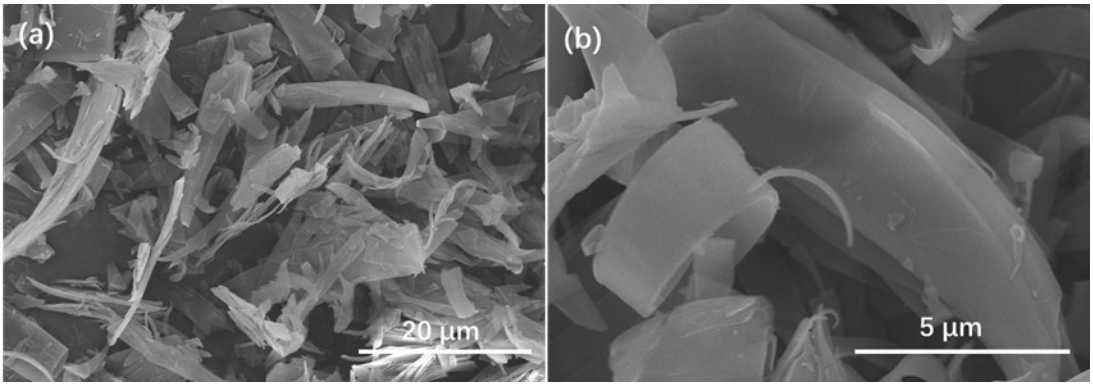

Fig. S2 (a, b) FESEM images of FA**.**

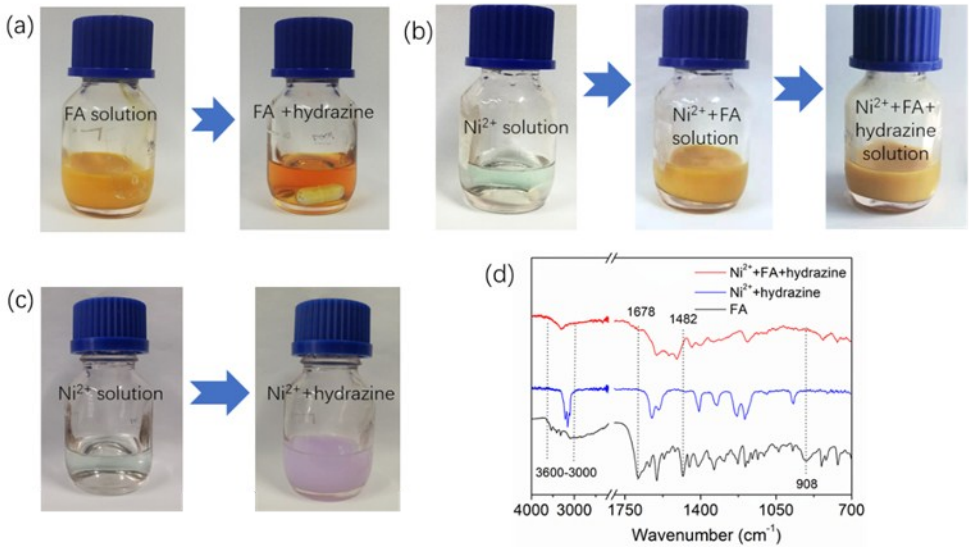

Fig. S3 Photo images of (a) FA-hydrazine and (b) Ni^{2+}-FA-hydrazine, (c) Ni^{2+}- hydrazine reaction processes in H_2O and ethanol mixture, and (d) the corresponding FTIR spectra of their products.

In comparison to FA, the markedly weakened ν (C=O) peak (1687 cm^{-1}) together with the absence of δ (O-H) peak (908 cm^{-1}) in the complex suggests the COO-Ni interaction. Meanwhile, the disappearance of pteridine ring peak (1482 cm^{-1}) and -NH_2 peak (in the range of 3600-3000 cm^{-1}) suggests a strong H bonding interaction between FA molecules in the complex. (References: *Int. J. Electrochem. Sci.*, 2011, **6**, 2943-2954; *J. Mater. Chem.*, 2012, **22**, 20291-20298)

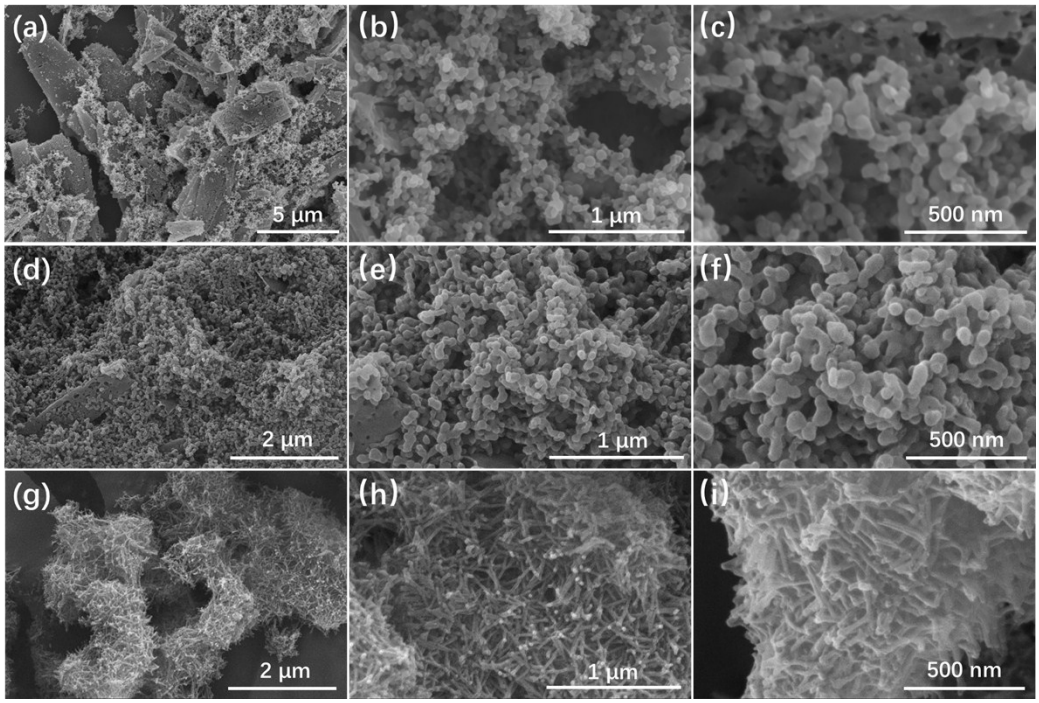

Fig. S4 FESEM images of Ni-FA complex products hydrothermally prepared at room temperature (a-c), 60°C (d-f) and 100°C (g-i).

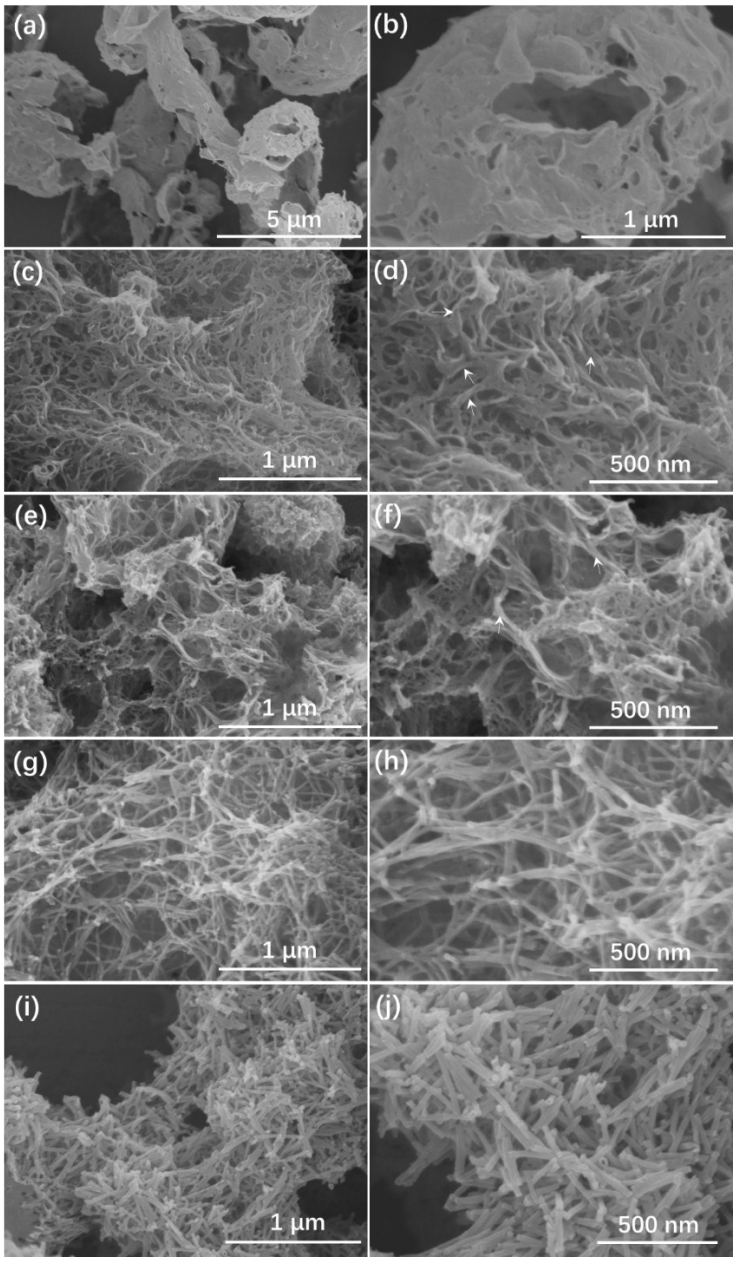

Fig. S5 SEM images of Ni-FA complex products prepared by addition of 0 mL (a, b), 0.2 mL (c, d), 0.5 mL (e, f), 1.5 mL (g, h) and 2.5 mL (i, j) hydrazine. The white arrows in (d) and (f) denote the curled nanobelts which tend to form nanotubes. The white arrows in (d) and (f) denote the nanobelts that tend to curl into nanotubes.

The length of resulting nanotubes is reduced while the volume of hydrazine being increased from 1.5 mL to 2.5 mL. It is possibly attributed to a burst formation of Ni-FA NTs, which results in limited FA and Ni^{2+} to sustain their growth in length.

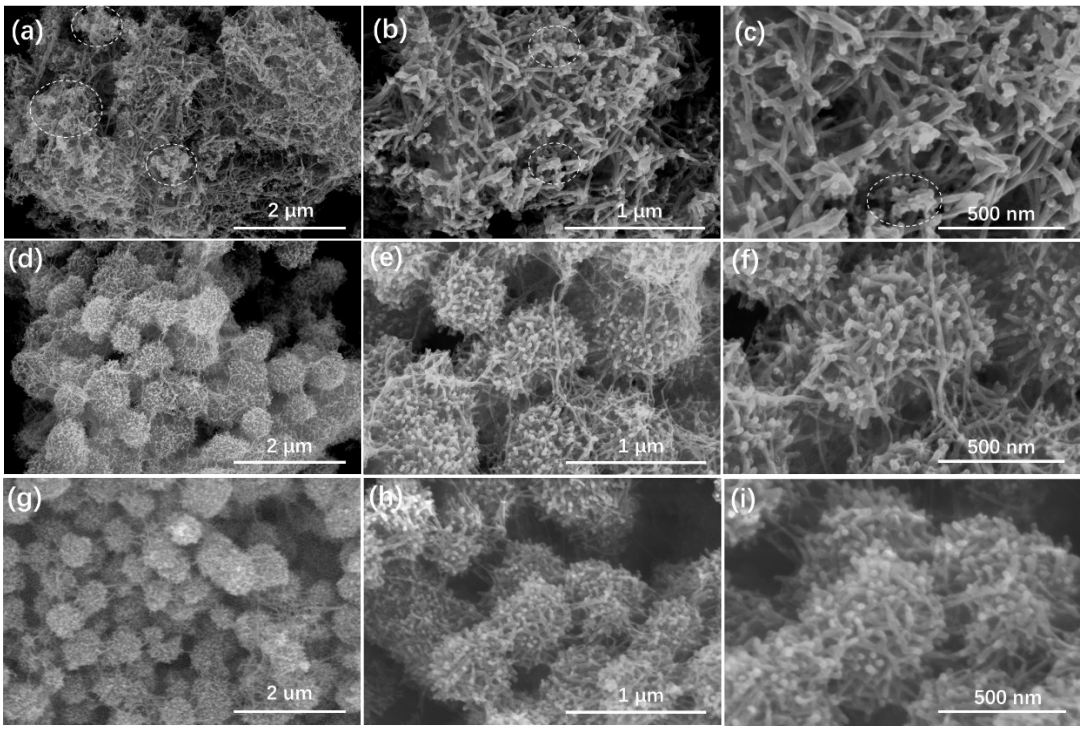

Fig. S6 Ni-FA complex products prepared at different Ni-to-FA (0.25 mmol) ratio, (a-c) 0.125 mmol $NiCl_2$, (d-f) 0.5 mmol $NiCl_2$ and (g-i) 1 mmol $NiCl_2$. The white circles in (a-c) denote the super short Ni-FA NTs (<100 nm in length).

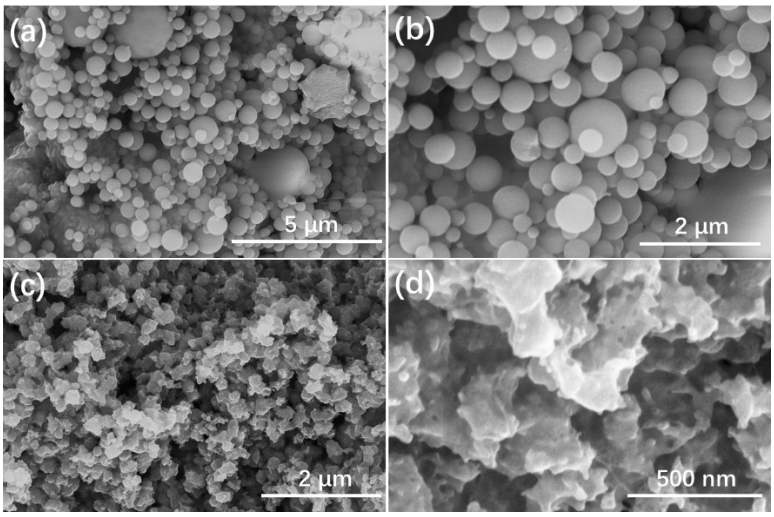

Fig. S7 FESEM images of Ni-FA complex products prepared in pure water (a, b) and pure ethanol (c, d).

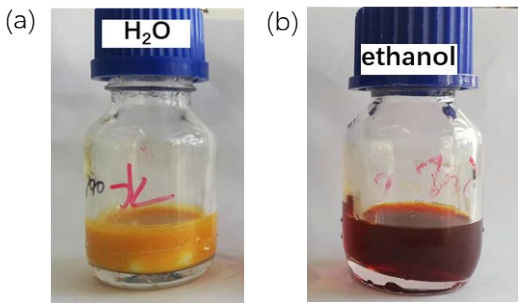

Fig. S8 Folic acid (0.25 mmol) in 13.5 mL (a) DI water and (b) ethanol after an ultrasonication treatment for 30 min.

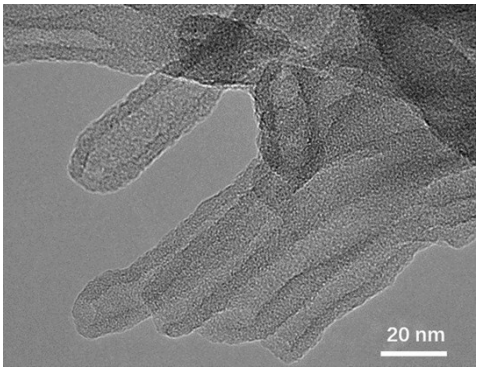

Fig. S9 HRTEM image of unwashed Ni-FA NTs.

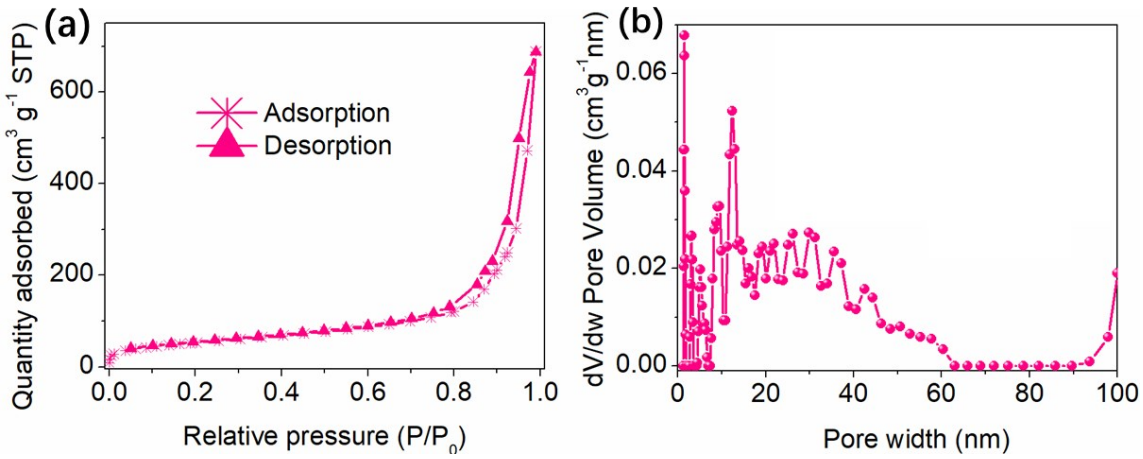

Fig. S10 (a) N_2 adsorption and desorption isotherm and (b) pore size distribution of Ni-FA NTs. The specific Brunauer-Emmett-Teller (BET) surface area of Ni-FA NTs is measured to be 190 m^2 g^{-1}. The pore size distribution curve in (b) shows a hierarchical micro-/meso-/macro-porous structure of Ni-FA NTs.

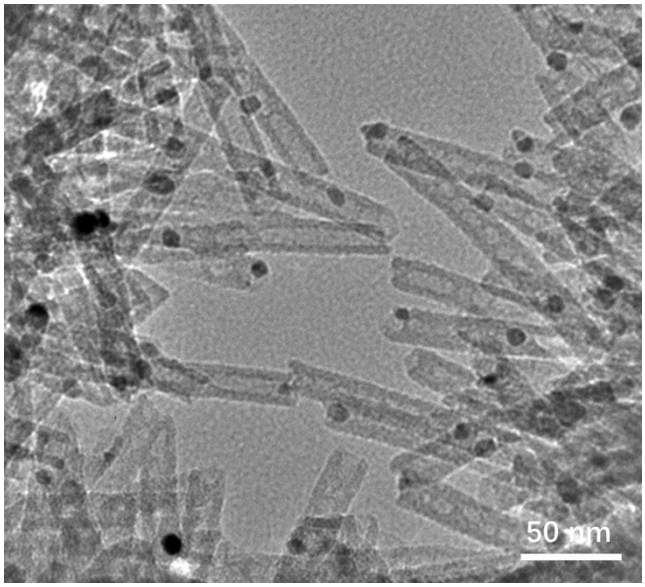

Fig. S11 TEM image of pod-like nanotubes obtained by thermal pyrolysis of Ni-FA NTs at 450 °C under N_2 for 2h.

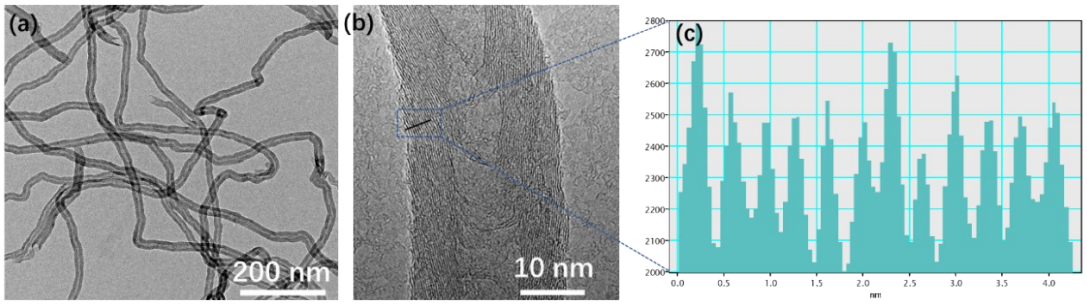

Fig. S12 TEM images (a and b) of commercial multi-wall carbon nanotube (MWCNT) sample and (c) line profiles of interlayer distances of graphene sheets extracted from image (b). The commercial MWCNT sample is obtained from Shenzhen Nanotech Port Co. Ltd and used for comparison. It possesses a typical diameter of 10~20 nm and a length larger than 5 μm. The average interlayer spacing of graphene sheets in the MWCNTs is measured in the range between 0.342 and 0.357 nm, representing the typical (002) plane of carbon. The sample has a specific surface area of 100~160 m^2 g^{-1}.

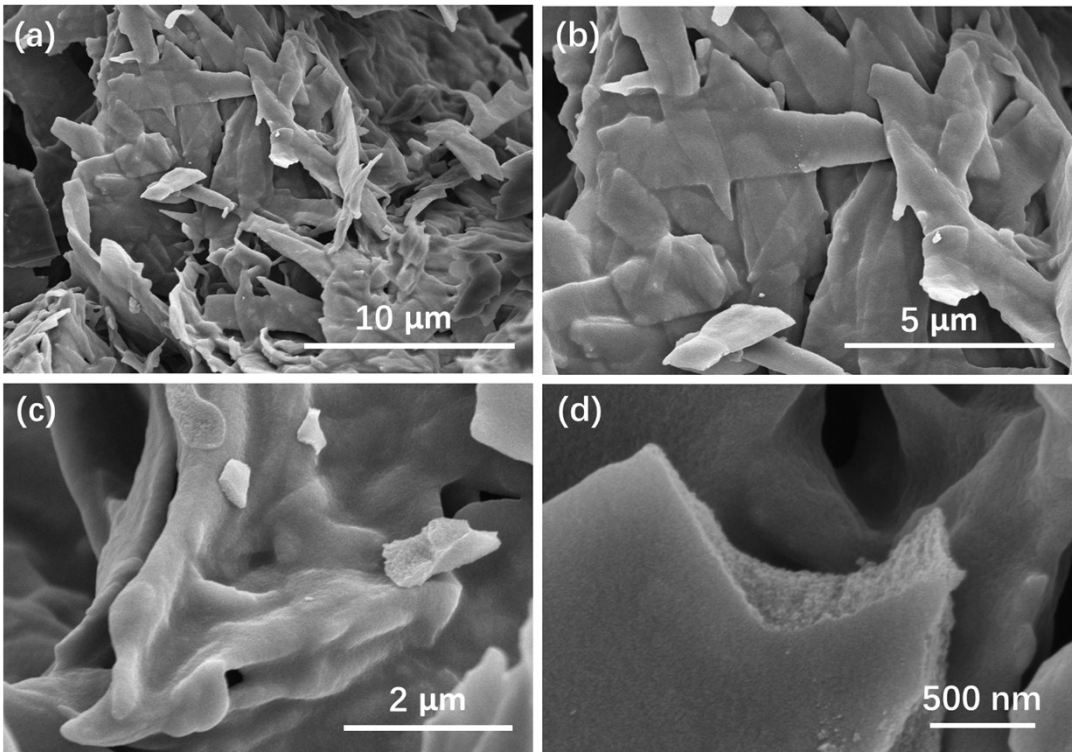

Fig. S13 (a-d) SEM images of N doped carbon (denoted as FA-900) obtained from the direct pyrolysis of FA at 900°C under N_2 for 2h.

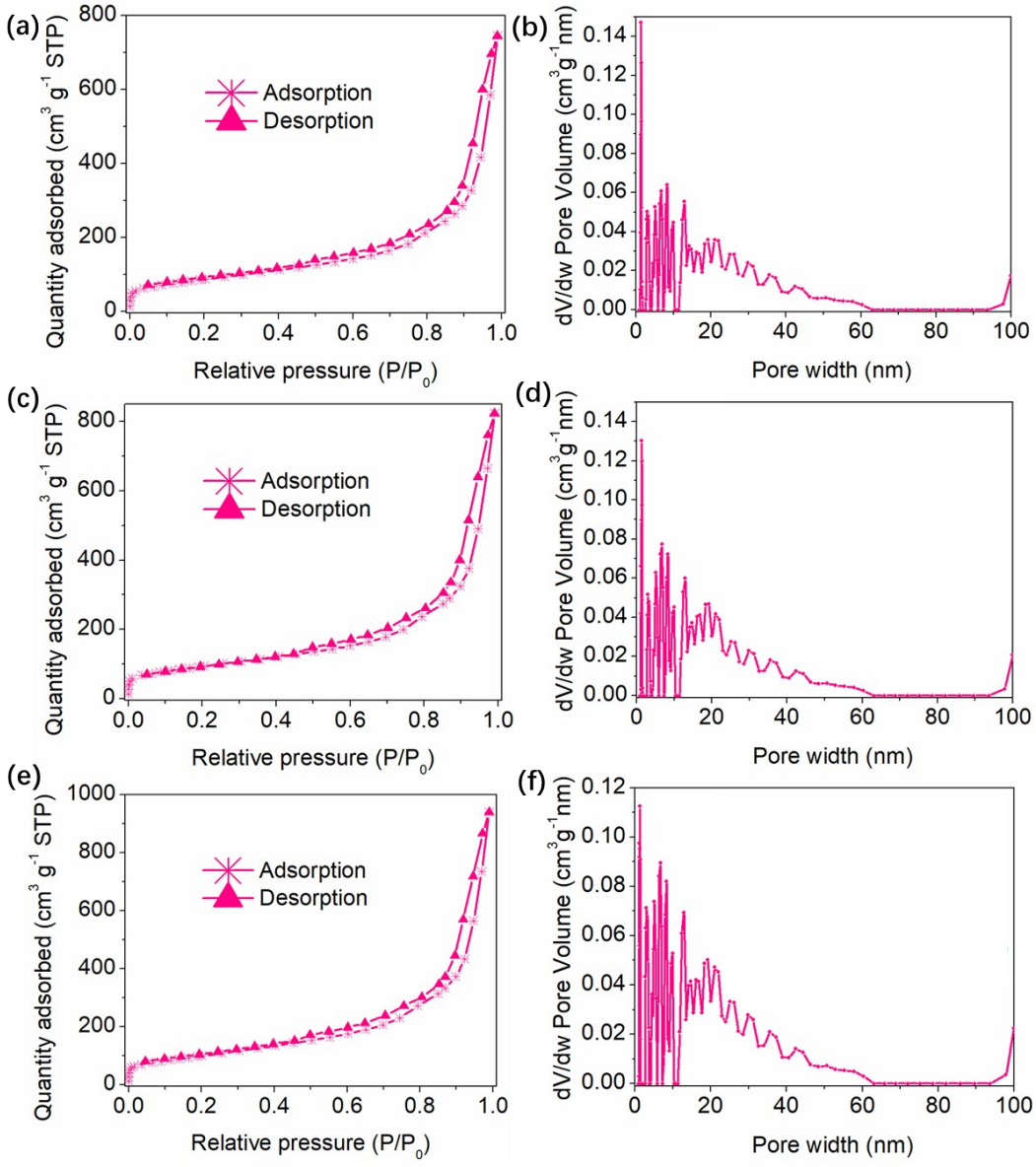

Fig. S14 N_2 adsorption/desorption isotherms of NiN_xCNT-700 (a), 800 (c) and 1000 (e) at 77 K. Pore size distribution of NiN_xCNT-700 (b), 800 (d) and 1000 (f).

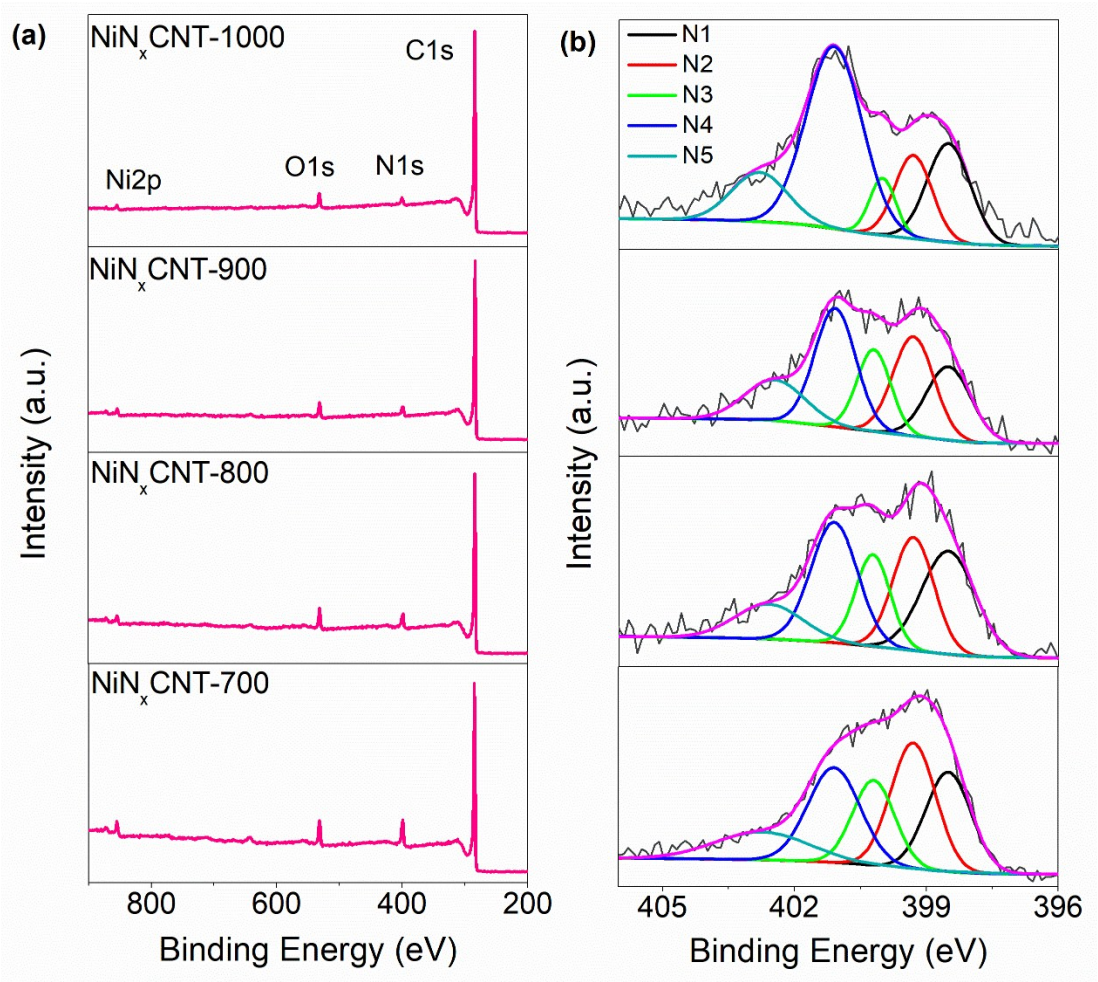

Fig. S15 XPS survey spectrum (a) and high-resolution N 1s spectra (b) of NiN_xCNT-700, 800, 900 and 1000. N1, N2, N3, N4 and N5 in (b) correspond to pyridinic N, Ni-N_x, pyrrolic, quaternary and oxidized pyridinic N, respectively. The content of C, N, Ni and O elements of NiN_xCNT samples are compared in Table S1.

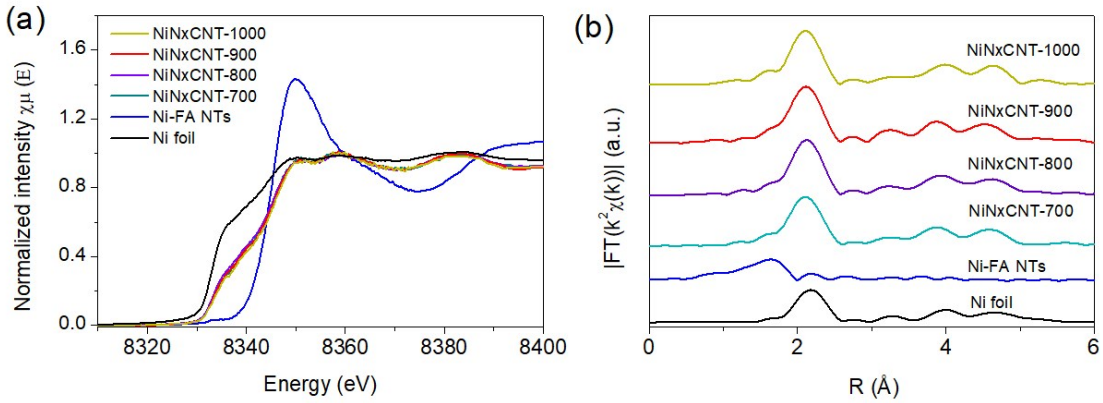

Fig. S16 (a) Ni K-edge XANES spectra and (b) Fourier transformed EXAFS spectra of NiNxCNT catalysts and the reference samples.

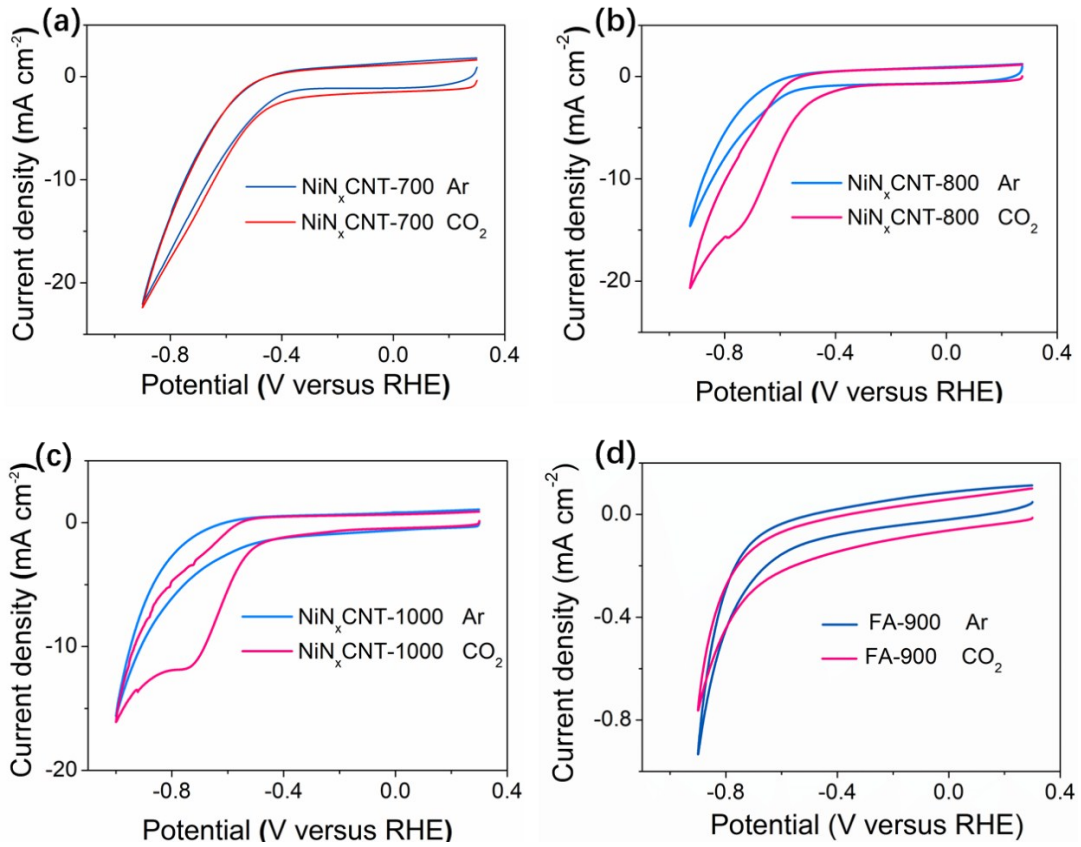

Fig. S17 Cyclic voltammetry (CV) of NiN_xCNT-700 (a), 800 (b), 1000 (c) and FA-900 (d) at 50 mV s^{-1} in Ar and CO_2-saturated 0.5 M $KHCO_3$ electrolyte.

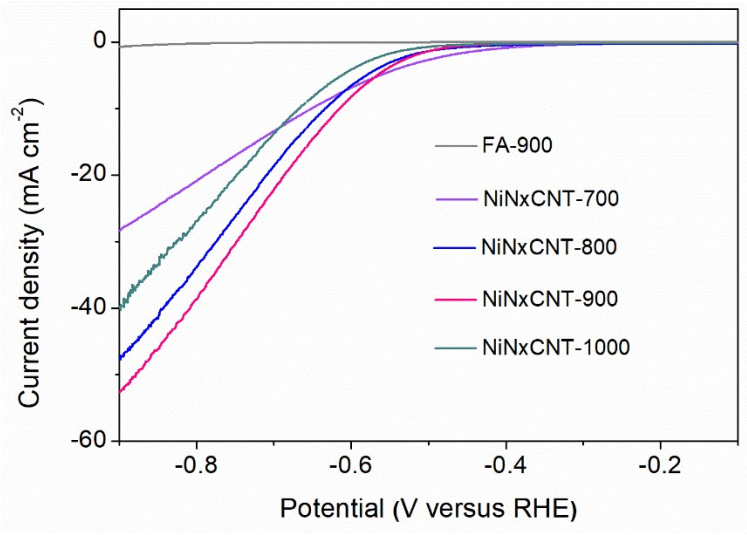

Fig. S18 *iR*-corrected linear sweep voltammetry (LSV) of the catalyst samples at a scan rate of 5 mV s^{-1} and rotating rate of 1600 rpm with a catalyst loading of 0.2 mg cm^{-2}.

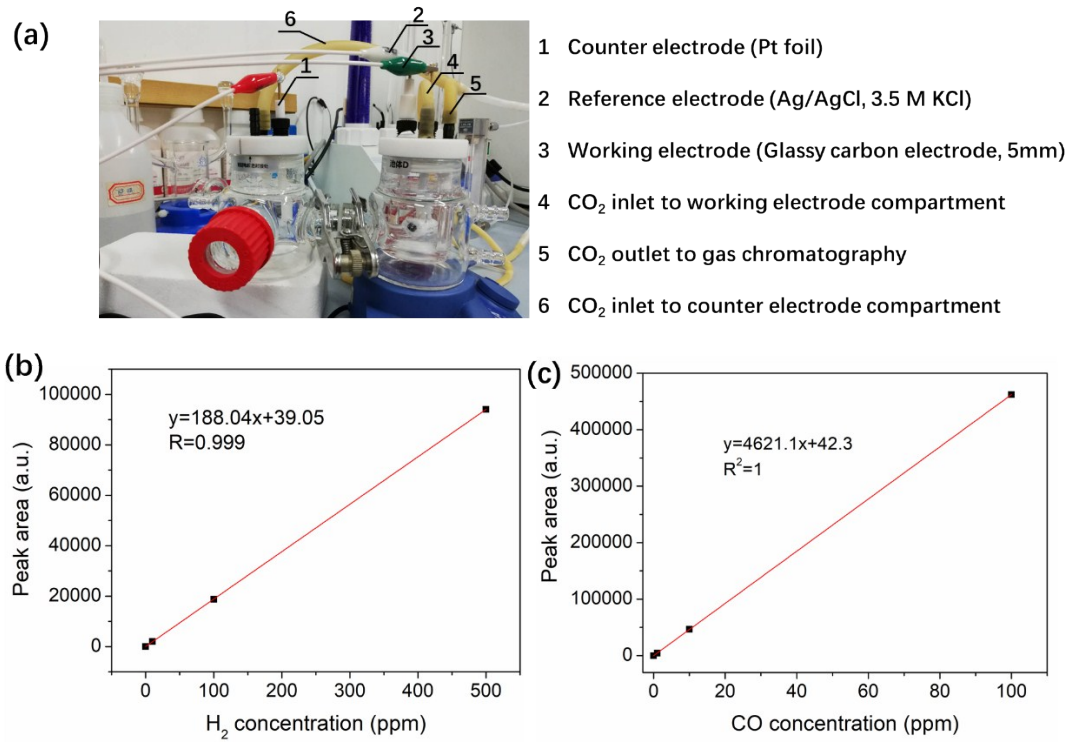

Fig. S19 (a) Photo image of gas-tight two-compartment H-cell used for CO_2 reduction. GC calibration curve for H_2 (b) and for CO (c).

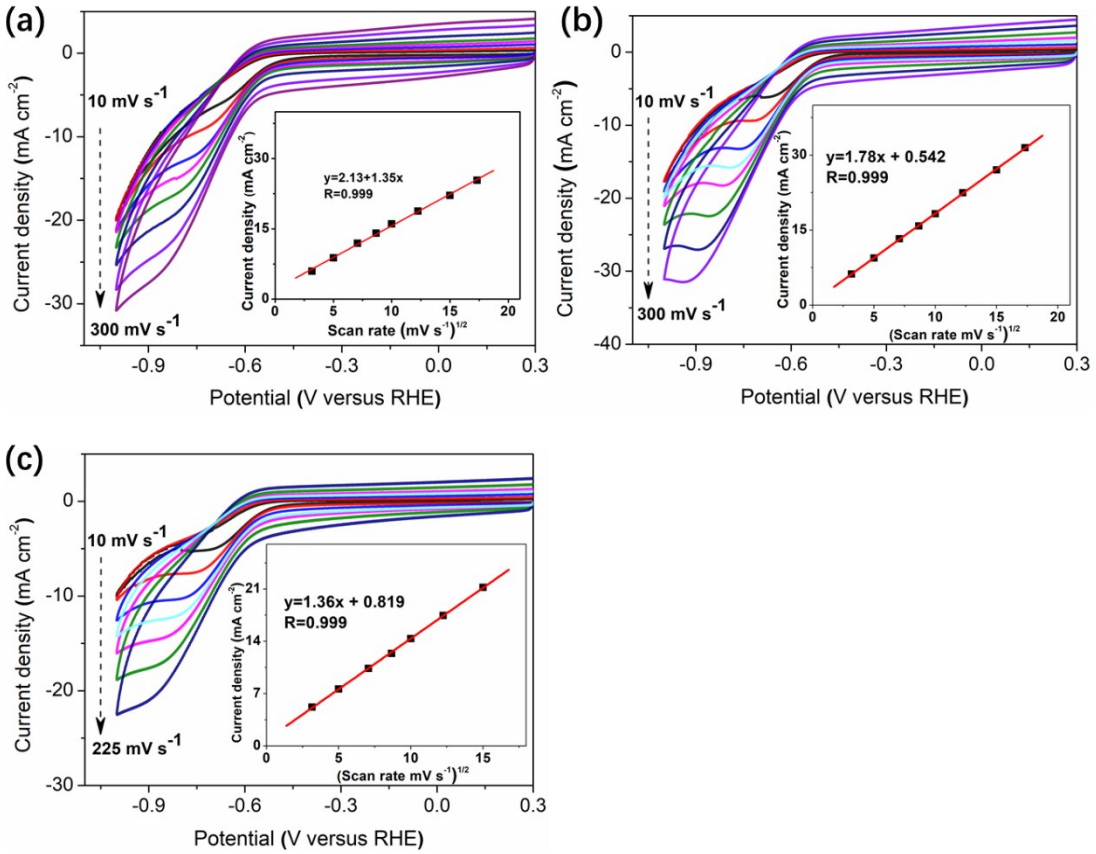

Fig. S20 Cyclic voltammetry (CV) of NiN_xCNT-800 (a), 900 (b) and 1000 (c) at scan rates of 10, 25, 50, 75, 100, 150, 225 and 300 mV s^{-1}. Inset shows the peak current versus $(\text{scan rate})^{1/2}$. The CV of NiN_xCNT-700 at different scan rates is not measured due to a poor stability.

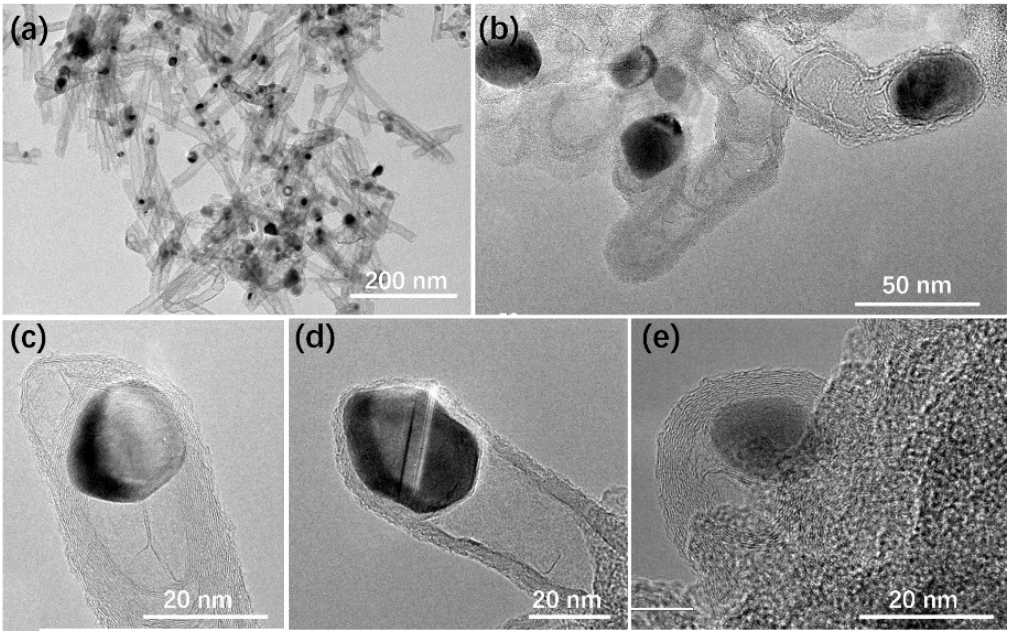

Fig. S21 TEM (a) and HRTEM (b-e) images of NiN_xCNT-900 at different positions.

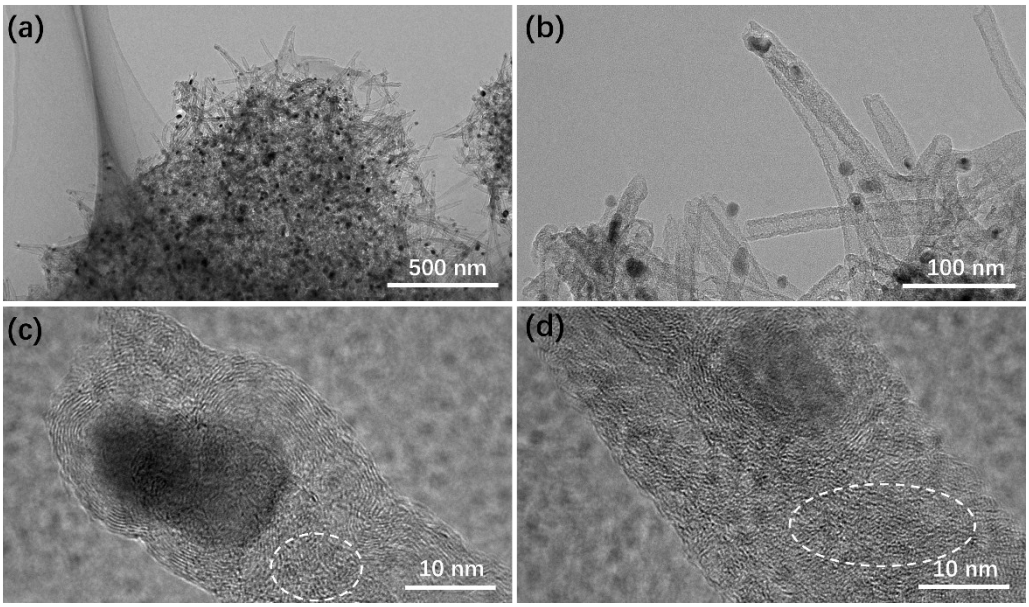

Fig. S22 (a-d) TEM images of NiN_xCNT-700 at different positions and magnifications. The white circles in (c) and (d) denote the highly disordered carbon lattice structure.

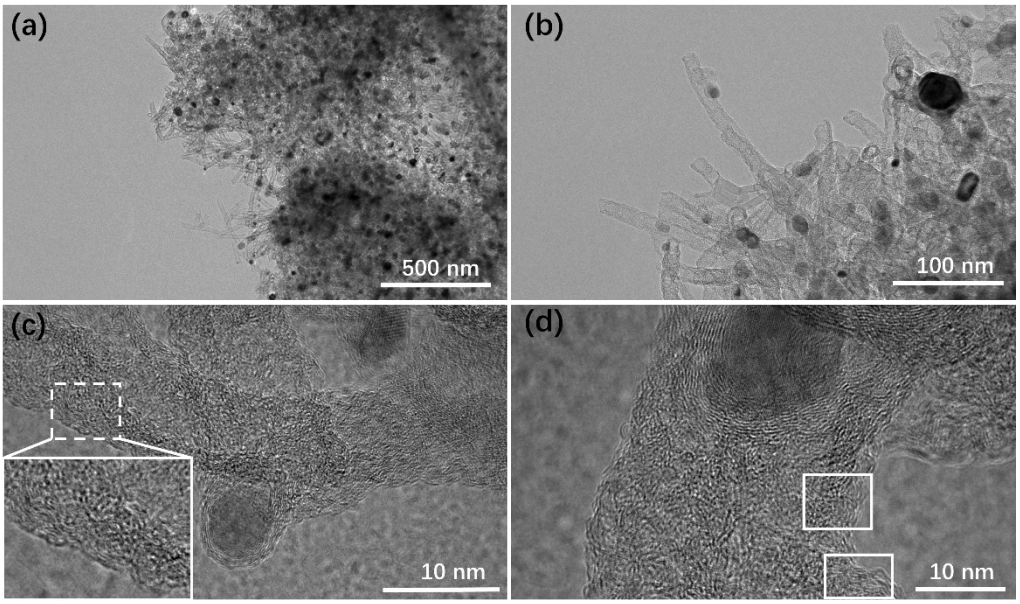

Fig. S23 (a-d) TEM images of NiN_xCNT-800 at different positions and magnifications. The white square in (c) and (d) denote the graphitic domains formed on the wall of CNTs.

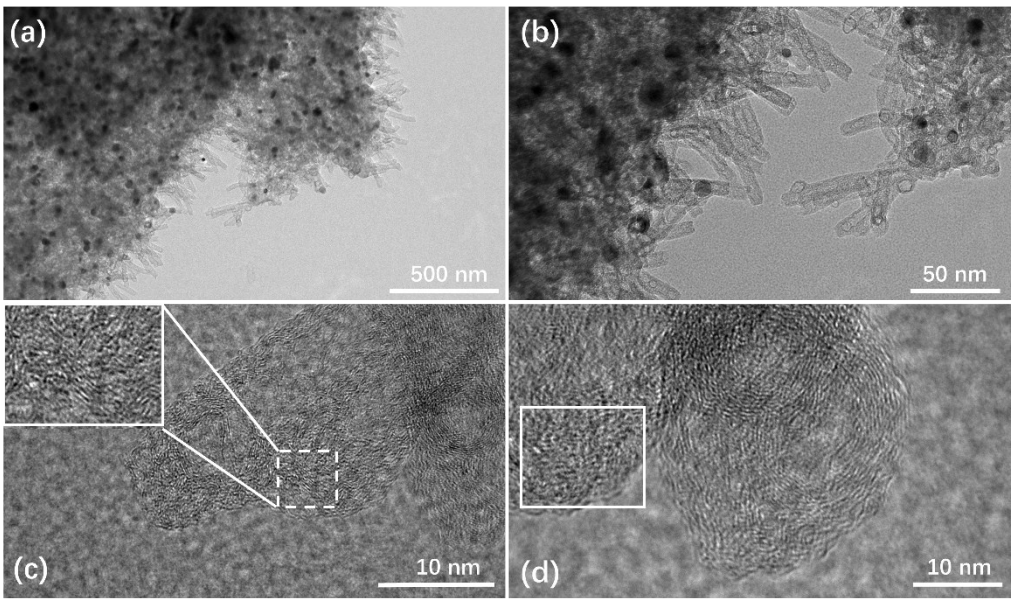

Fig. S24 (a-d) TEM images of NiN_xCNT-900 at different positions and magnifications. The white square in (c) and (d) denote the graphitic domains formed on the wall of CNTs.

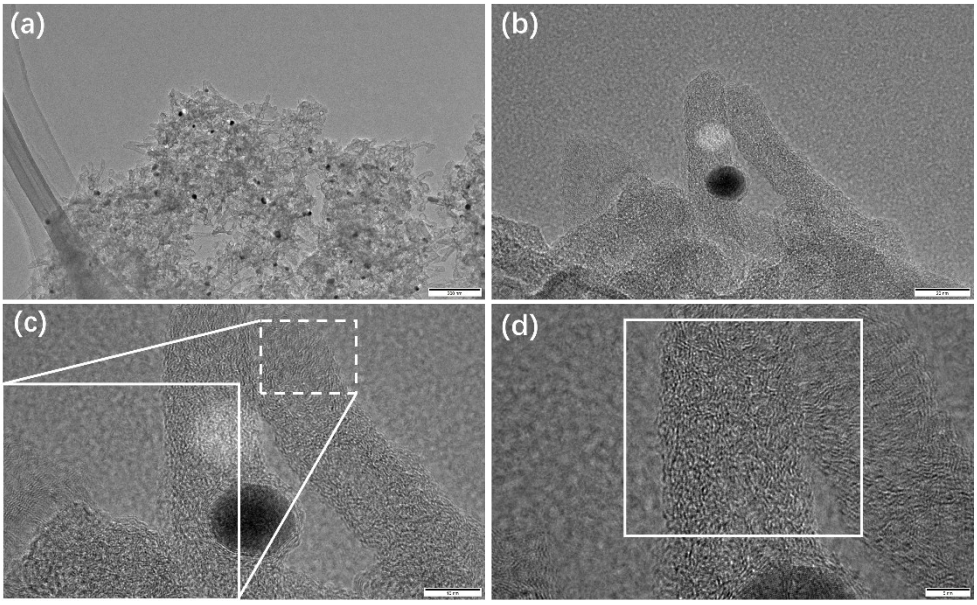

Fig. S25 (a-d) TEM images of NiN_xCNT-1000 at different positions and magnifications. The white square in (c) and (d) denote the graphitic domains formed on the wall of CNTs.

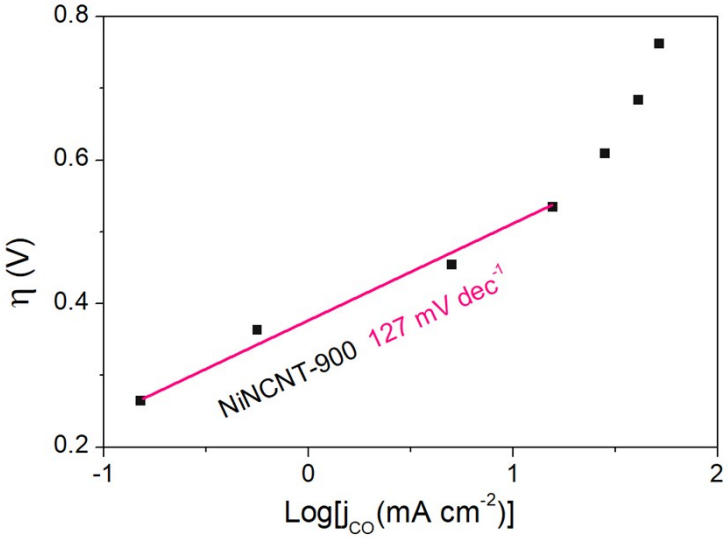

Fig. S26 CO Tafel plot of NiN_xCNT-900.

Tab. S1 Elemental composition (XPS), specific area (BET) and Ni content (TGA) comparison of NiN_xCNT catalsyts prepared at different pyrolysis temperature.

Element	NiN_xCNT-700	NiN_xCNT-800	NiN_xCNT-900	NiN_xCNT-1000
Elemental composition (at%) [From Fig. S15]				
C (at%)	80.75	85.82	89.21	92.26
N (at%)	11.41	7.46	5.66	3.47
Ni (at%)	1.15	0.82	0.59	0.45
O (at%)	6.7	5.89	4.53	3.82
Relative concentration of N functionalities (%) [From Fig. S15]				
Pyridinic N	21.27	25.97	18.89	19.14
Ni-N_x	26.51	21.83	23.43	14.40
Pyrrolic N	16.73	14.82	15.78	6.66
Graphitic N	23.27	26.40	27.93	47.43
N-O	12.22	10.98	13.96	12.38
Specific area (m^2g^{-1}) [From Fig. 4d and S14]				
BET surface area	310.6	333.9	314.4	369.4
Micropore area	254.2	267.0	238.8	268.9
Content of Ni (wt%) [From TGA measurements]				
Ni	33.7	30.4	27.9	24.2

Tab. S2 Comparison of the NiN_xCNT-900 catalyst with recently reported high-performance transition metal-based and noble metal-based electrocatalsyts for CO_2 reduction to CO.

Catalyst	Precursors	j_{CO} (mA cm^{-2})	Potential (V versus RHE) [a]	Catalyst loading (mg cm^{-2})	Electrolyte (pH)	Maximum FE_{CO} (%)	Ref. [b]
NiN_x CNT-900	Bioligand-Ni^{2+} complex	9.0	-0.68	0.2	0.5 M $KHCO_3$ (7.2)	98.3 (-0.68~-0.98 V)	This work
Ni SAs/ NCNTs	ZIF-8+DCD+ Ni^{2+}	~10	-0.70	0.8	0.5 M $KHCO_3$ (7.2)	97 (-0.9~-1.0 V)	19
Ni-N-graphene	GO+Ni^{2+}+NH_3	~5.0	-0.80	0.2	0.5 M $KHCO_3$ (7.2)	~90	38
Ni-N-MEGO	Graphene+Ni +urea+NH_3	~27.0	-0.70	0.5	0.5 M $KHCO_3$ (7.2)	92.1	20
Ni-N-C	Urea+citritic acid+Ni^{2+}	~8.2	-0.75	0.3	0.1 M KHCO3 (6.8)	96 (-0.75 V)	15
Ni SAs/N-C	Ni^{2+}-exchanged ZIF8	~7.5	-1.0	0.2	0.5 M $KHCO_3$ (7.2)	~70	19
Fe-N-graphene	GO+Fe^{3+}+NH_3	~1.7	-0.60	1.0	0.1 M $KHCO_3$ (6.8)	80	47
Fe-N-CNTs	Graphene/Fe^{3+} +melamine+IL	~2.8	-0.66	2.0	0.1 M $KHCO_3$ (6.8)	95.8 (-0.66 V)	48
$Ni-N_4-C$	Ni doped g-C_3N_4 + glucose	28.6	-0.81	0.2	0.5 M $KHCO_3$ (7.2)	99 (-0.71~0.91 V)	49
Ni(I)-N-graphene	Melamine + L-alanine + Ni^{2+}	~10	-0.50	0.4	0.5 M KHCO3 (7.3)	97 (-0.5~-0.7 V)	14
Au nanowire	$HAuCl_4$	~8.2	-0.35	81.6	0.5 M $KHCO_3$ (7.2)	94	7
Porous Ag	Ag-Al alloy	~8.7	-0.50	-	0.5 M $KHCO_3$ (7.2)	92	50

[a] The potential value corresponds to the potential that obtains the j_{co} in the 2nd column.

[b] The references can be found in the manuscript.